OPTIMUM EXPERIMENTAL DESIGN BY SHAPE OPTIMIZATION OF SPECIMENS IN LINEAR ELASTICITY[*]

TOMMY ETLING[†] AND ROLAND HERZOG[†]

Abstract. The identification of Lamé parameters in linear elasticity is considered. An optimum experimental design problem is formulated, which aims at minimizing the size of an associated confidence ellipsoid by optimizing the shape of the specimen. Representations of the Eulerian shape derivative and the shape gradient are derived by means of shape calculus and adjoint techniques. Numerical experiments are conducted, yielding specimens of improved shape.

1. Introduction. Optimum experimental design (OED) is a well established technique which aims at improving experimental setups in order to increase the precision of parameter estimation in the face of measurement errors. To date, OED is still mostly used for models which are described by ordinary differential equations or differential-algebraic equations, e.g., in chemical engineering and biology; see, for instance, [26, 2], [9, Chapter 7] for recent contributions. In this context, typical experimental conditions, which serve as optimization variables, include initial conditions, right-hand side sources, and observation times. Extensions of OED to models involving partial differential equations were considered, for instance, in [14, 30, 4, 17, 10, 1, 12, 11].

In this paper, we consider an OED problem in linear elasticity, where the model is described by an elliptic partial differential equation. In a typical experimental setup the two Lamé parameters, which determine the constitutive behavior of the material in the isotropic case, are to be identified from the response of a specimen subjected to tensile stress. Our objective is to increase the precision in the estimation of these parameters, expressed here in terms of the A-criterion applied to the Fisher information matrix.

The main novelty of our approach is that we treat the shape of the specimen as an experimental condition. Following the Lagrangian strategy for shape optimization problems of [5, 7], recently revisited by [29, 18], we derive a volume representation of the Eulerian shape derivative of the OED objective. Similar to other classical approaches as in [27], the Lagrangian approach leads to an adjoint-based representation of the shape derivative, but it avoids material or local shape derivatives of the state. As in [25], we then employ the volume representation of the shape derivative to obtain a shape gradient w.r.t. an H^1-based inner product, which drives a gradient descent algorithm. Numerical experiments demonstrate the viability of our approach and reveal new and interesting specimen shapes for tensile experiments.

[†]Faculty of Mathematics, Professorship Numerical Mathematics (Partial Differential Equations), Technische Universität Chemnitz, D–09107 Chemnitz, Germany (tommy.etling@mathematik.tu-chemnitz.de, https://www.tu-chemnitz.de/mathematik/part_dgl/people/etling, roland.herzog@mathematik.tu-chemnitz.de, https://www.tu-chemnitz.de/herzog).

We are aware of only one publication where geometry was used as an experimental condition. In [19], the boundary of a measurement device was discretized by a small number of shape parameters and optimized using a derivative-free optimization approach to improve the estimation precision of two unknown parameters in a Bingham flow model.

The material is organized as follows. In section 2, we describe the parameter estimation problem under consideration for a given shape of the specimen. We also quantify the estimation accuracy in terms of the A-criterion applied to the Fisher information matrix, which subsequently serves as our optimality criterion. Section 3 is devoted to the shape optimization problem and it contains as our main result the volume representation of the Eulerian shape derivative as well as the H^1-based shape gradient. Numerical experiments in two space dimensions are presented in section 4. We conclude with an outlook in section 5.

2. Parameter estimation in linear elasticity. In this section we briefly review parameter estimation problems in linear elasticity with infinitesimal strains. We refer to [3] for an overview from the mathematical point of view and to [6] from the engineering perspective. We focus on the deformation of an elastic specimen by the application of certain boundary stresses or boundary displacements. We measure the mean values of the displacement field in a number of predefined observation areas distributed across the specimen's surface. In practice, this is achieved by optical measurement techniques such as video extensometers. The constitutive parameters are subsequently identified from the measured material response by way of a least-squares approach.

In this paper we concentrate on prismatic specimens with two-dimensional (2D) displacement fields, but extensions to fully 3D bodies are clearly possible. Other types of measurements such as strain gauges are possible as well but they will not be discussed here. In the interest of clarity of the presentation, we focus primarily on a single stress-driven experiment with given boundary traction.

2.1. Forward problem. Let us denote by $\Omega \subset \mathbb{R}^2$ the lateral cross section of the elastic specimen; see Figure 1. The state variable of the problem is the displacement field $\boldsymbol{u} : \Omega \to \mathbb{R}^2$. We denote by $D\boldsymbol{u}$ the Jacobian of $\boldsymbol{u}$ and by

$$\boldsymbol{\varepsilon}(\boldsymbol{u}) = \frac{1}{2}\big(D\boldsymbol{u} + (D\boldsymbol{u})^\top\big) = \mathrm{sym}(D\boldsymbol{u})$$

the (linearized) strain tensor. Here and throughout the rest of the paper, "sym" denotes the symmetric part of a matrix.

The forward problem of linear elasticity is described by the equilibrium of forces (gravity is neglected),

$$(2.1) \qquad\qquad -\operatorname{div}\boldsymbol{\sigma} = \boldsymbol{0} \quad \text{in } \Omega,$$
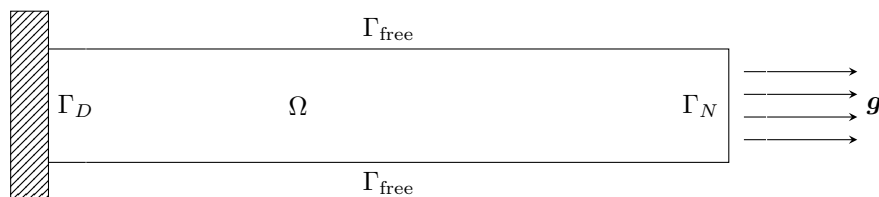

FIG. 1. *Typical configuration of a specimen in a tensile experiment.*

together with mixed boundary conditions

(2.2a) $$\boldsymbol{\sigma}\boldsymbol{n} = \boldsymbol{g} \quad \text{on } \Gamma_N,$$

(2.2b) $$\boldsymbol{\sigma}\boldsymbol{n} = \boldsymbol{0} \quad \text{on } \Gamma_{\text{free}},$$

(2.2c) $$\boldsymbol{u} = \boldsymbol{0} \quad \text{on } \Gamma_D.$$

Herein, $\boldsymbol{\sigma} : \Omega \to \mathbb{R}^{2\times2}_{\text{sym}}$ denotes the stress field with values in the symmetric matrices of dimension 2×2. The differential operator div denotes the (rowwise) divergence.

The boundary Γ is divided into three disjoint parts, the traction boundary Γ_N, the force-free boundary Γ_{free}, and the clamping boundary Γ_D. Moreover, $\boldsymbol{n}$ is the outer unit normal along the boundary Γ. The data $\boldsymbol{g}$ accounts for the applied tensile stress during the experiment; see again Figure 1.

In linear elasticity the relation between stresses $\boldsymbol{\sigma}$ and strains $\boldsymbol{\varepsilon}(\boldsymbol{u})$ is described by a linear mapping from $\mathbb{R}^{2\times2}_{\text{sym}}$ into itself. The latter is represented by the fourth-order elasticity tensor $\mathbb{C}$, i.e.,

(2.3) $$\boldsymbol{\sigma} = \mathbb{C}\,\boldsymbol{\varepsilon}(\boldsymbol{u})$$

holds pointwise in Ω. The specific form of $\mathbb{C}$ in the isotropic case is addressed in subsection 2.2.

We will work with the well-known weak formulation of the state equation (2.1)–(2.3),

(2.4) Find $\boldsymbol{u} \in \mathcal{V}$ such that $\displaystyle\int_\Omega \boldsymbol{\varepsilon}(\boldsymbol{v}) : \mathbb{C}\,\boldsymbol{\varepsilon}(\boldsymbol{u})\,\mathrm{d}\boldsymbol{x} = \int_{\Gamma_N} \boldsymbol{g} \cdot \boldsymbol{v}\,\mathrm{d}\boldsymbol{s}$ for all $\boldsymbol{v} \in \mathcal{V}$.

In (2.4), the standard inner product (associated with the Frobenius norm $|\cdot|_F$) between matrices of equal size is defined by $A : B := \text{trace}(A^\top B)$. The state and test space in (2.4) is given by

$$\mathcal{V} := H^1_D(\Omega)^2 := \{\boldsymbol{u} \in H^1(\Omega)^2 : \boldsymbol{u} = \boldsymbol{0} \text{ on } \Gamma_D\}.$$

Provided that $\mathbb{C}$ is coercive, i.e.,

$$\boldsymbol{\varepsilon} : \mathbb{C}\,\boldsymbol{\varepsilon} \geq c\,|\boldsymbol{\varepsilon}|^2_F \text{ for all } \boldsymbol{\varepsilon} \in \mathbb{R}^{2\times2}_{\text{sym}}$$

with some constant $c > 0$, it follows from the Lax–Milgram theorem and Korn's inequality that (2.4) is uniquely solvable and that the solution depends continuously on the data $\boldsymbol{g}$, for instance, w.r.t. the topologies of $L^2(\Gamma_N)^2$ and $H^1(\Omega)^2$.

2.2. Identification problem. We will be concerned with the case of homogeneous, isotropic elasticity, when $\mathbb{C}$ is described by only two parameters. One common parametrization uses the Lamé coefficients (λ, μ) with $\mu > 0$ and $\lambda + \mu > 0$:

(2.5) $$\mathbb{C}\,\boldsymbol{\varepsilon} = 2\,\mu\,\boldsymbol{\varepsilon} + \lambda\,\text{trace}(\boldsymbol{\varepsilon})\,\text{id}_{2\times2}\,.$$

The second parameter μ is also known as the shear modulus. We mention that we consider the so-called plane-stress situation, i.e., the specimen can move freely in thickness direction. This will play a role later on.

Clearly, it is impossible to measure the entire displacement state. In practical experiments, one encounters, for instance, measurements of the displacement of selected points of the specimen, as well as measurements of certain strain components. We
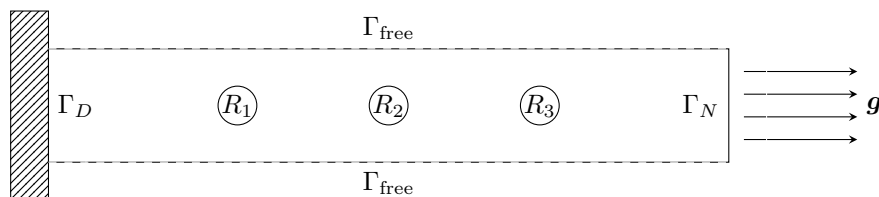
FIG. 2. *Simplified configuration of a specimen with measurement regions R_k ($k = 1, 2, 3$) and Γ_{free} (dashed lines) subject to shape optimization on Γ_{free}.*

concentrate here on measurements of the average displacement vector over a number of small observation regions distributed across the specimen's lateral surface. Since we consider a 2D situation, this amounts to interior measurements of the form

$$(2.6) \qquad M_k \, \boldsymbol{u} = \frac{1}{|R_k|} \int_{R_k} \boldsymbol{u} \cdot \boldsymbol{e}_k \, \mathrm{d}\boldsymbol{x}, \quad k = 1, \ldots, n_{\mathrm{meas}}.$$

Each measurement k belongs to a measurement region $R_k \subset \Omega$ and a measurement direction $\boldsymbol{e}_k$, usually $\boldsymbol{e}_k = (1, 0)^\top$ or $\boldsymbol{e}_k = (0, 1)^\top$. The number of these measurements is denoted by n_{meas}. It is not necessary that the measurement regions be disjoint, although this will be the case in our numerical experiments; see Figure 2.

The most common approach for the estimation of the elastic parameters (λ, μ) is based on a least-squares formulation. We assume that each measurement (2.6) is subject to a normally distributed measurement error with zero mean and variance σ_k^2. We also assume that the measurement errors are independent, i.e., the joint measurement covariance matrix

$$\Sigma = \mathrm{diag}(\sigma_k^2), \quad k = 1, \ldots, n_{\mathrm{meas}}$$

is diagonal.

Let us denote by η_k the individual measurements, $k = 1, \ldots, n_{\mathrm{meas}}$. Then the maximum likelihood estimator for the elastic parameters is equivalent to the solution of the following weighted least-squares problem,

$$(2.7) \qquad \text{Minimize} \quad f(\boldsymbol{p}, \boldsymbol{u}) = \frac{1}{2} \sum_{k=1}^{n_{\mathrm{meas}}} \sigma_k^{-2} (M_k \, \boldsymbol{u} - \eta_k)^2, \quad (\boldsymbol{p}, \boldsymbol{u}) \in P \times \mathcal{V},$$

subject to $\boldsymbol{u}$ solving the forward problem (2.4).

Herein, $\boldsymbol{p}$ corresponds to the pair (λ, μ). Moreover, P denotes the open subset of admissible parameters, i.e.,

$$P = \{(\lambda, \mu) \in \mathbb{R}^2 : \mu > 0, \ \lambda + \mu > 0\}.$$

In place of the constrained problem (2.7) it will be convenient to consider the reduced problem, which depends only on $\boldsymbol{p}$. To this end we introduce the parameter-to-state map

$$(2.8) \qquad \mathbb{R}^2 \supset P \ni \boldsymbol{p} \mapsto \mathcal{S}(\boldsymbol{p}) = \boldsymbol{u} \in \mathcal{V},$$

where $\boldsymbol{u}$ solves (2.4). Since S is well defined, the reduced problem becomes

$$(2.9) \qquad \text{Minimize} \quad \mathcal{F}(\boldsymbol{p}) := f(\boldsymbol{p}, \mathcal{S}(\boldsymbol{p})) = \frac{1}{2} \sum_{k=1}^{n_{\mathrm{meas}}} \sigma_k^{-2} (M_k \, \mathcal{S}(\boldsymbol{p}) - \eta_k)^2, \quad \boldsymbol{p} \in P.$$

We emphasize that (2.9) is a *nonlinear* least-squares problem despite the linear measurements and the linearity of the state equation since the unknown parameter vector $\boldsymbol{p}$ enters (2.4) through the coefficients and thus S is nonlinear.

2.3. Sensitivity equation. Let us denote by

$$(2.10) \qquad r_k := M_k\,\mathcal{S}(\boldsymbol{p}) - \eta_k, \quad k = 1, \ldots, n_{\text{meas}}$$

the (unweighted) residuals of (2.9). For the efficient solution of (2.9), but also for the subsequent assessment of the accuracy of the estimation, we consider the Jacobian J of the residual vector w.r.t. $\boldsymbol{p} = (p_1, p_2)$. Since the measurement operators M_k are linear, we get

$$(2.11) \qquad J_{k,\ell}(\boldsymbol{p}) := M_k\,\frac{\partial}{\partial p_\ell}\mathcal{S}(\boldsymbol{p}), \quad k = 1, \ldots, n_{\text{meas}},\ \ell = 1, 2.$$

By the implicit function theorem and (2.4), we obtain that the sensitivity of the displacement field w.r.t. to either of the two parameters, $\delta\boldsymbol{u}_\ell := \frac{\partial}{\partial p_\ell}\mathcal{S}(\boldsymbol{p})$, is defined by the unique solution of the following linearized problem:

$$(2.12)$$

Find $\delta\boldsymbol{u}_\ell \in \mathcal{V}$ such that $\displaystyle\int_\Omega \boldsymbol{\varepsilon}(\boldsymbol{v}) : \mathbb{C}\,\boldsymbol{\varepsilon}(\delta\boldsymbol{u}_\ell)\,\mathrm{d}\boldsymbol{x} = -\int_\Omega \boldsymbol{\varepsilon}(\boldsymbol{v}) : \mathbb{C}_\ell\,\boldsymbol{\varepsilon}(\boldsymbol{u})\,\mathrm{d}\boldsymbol{x}$ for all $\boldsymbol{v} \in \mathcal{V}$,

where $\boldsymbol{u} = \mathcal{S}(\boldsymbol{p})$. Here we used the abbreviation $\mathbb{C}_\ell := \frac{\partial}{\partial p_\ell}\mathbb{C}$, and according to (2.5) we have

$$(2.13\text{a}) \qquad \mathbb{C}_\lambda\,\boldsymbol{\varepsilon} := \frac{\partial}{\partial\lambda}\mathbb{C}\,\boldsymbol{\varepsilon} \equiv \text{trace}(\boldsymbol{\varepsilon})\,\text{id}_{2\times2},$$

$$(2.13\text{b}) \qquad \mathbb{C}_\mu\,\boldsymbol{\varepsilon} := \frac{\partial}{\partial\mu}\mathbb{C}_\mu \equiv 2\,\boldsymbol{\varepsilon}.$$

By plugging in the specific form of the measurement operator (2.6), we infer that the entries in the Jacobian (2.11) become

$$(2.14) \qquad J_{k,\ell}(\boldsymbol{p}) = \frac{1}{|R_k|}\int_{R_k}\delta\boldsymbol{u}_\ell \cdot \boldsymbol{e}_k\,\mathrm{d}\boldsymbol{x}, \quad k = 1, \ldots, n_{\text{meas}},\ \ell = 1, 2.$$

ASSUMPTION 2.1. *We assume throughout that the Jacobian has rank two, i.e., that both parameters are, in principle, identifiable from the measurements available.*

This assumption does not impose severe restrictions on the measurement setup.

2.4. Accuracy of estimation. Intuitively, parameters in a model can be well identified if their change leads to a significant model response, or more precisely, a significant response in the *observed* part of the model. This information is encoded in the Jacobian J (2.11) of the residuals. We follow here a classical approach and assess the accuracy of the estimation based on the Fisher information matrix (also known as the precision matrix)

$$(2.15) \qquad F(\boldsymbol{p}) = J(\boldsymbol{p})^\top \Sigma^{-1} J(\boldsymbol{p}) \in \mathbb{R}^{2\times2}.$$

We refer the reader to [30, 23, 22, 9] for in-depth material on this topic. Notice that the Fisher information matrix at $\boldsymbol{p}$ coincides with the inverse of the covariance of the

least-squares estimator when the residuals are linearized about $\boldsymbol{p}$; see, for instance, [9, Chapter 1.4.2]. We therefore denote this covariance matrix by

$$(2.16) \qquad C(\boldsymbol{p}) = F(\boldsymbol{p})^{-1} \in \mathbb{R}^{2 \times 2}.$$

Notice that the inverse exists due to Assumption 2.1.

Common criteria assessing the precision of the estimation, based on the eigenvalues $\{\lambda_\ell\}$ of the respective 2×2 covariance matrix C, are

$$(2.17a) \qquad a\text{A-criterion} \quad \psi_A(C) = \frac{1}{2} \sum_{\ell=1}^{2} \lambda_\ell = \frac{1}{2} \operatorname{trace} C,$$

$$(2.17b) \qquad b\text{D-criterion} \quad \psi_D(C) = \left(\prod_{\ell=1}^{2} \lambda_\ell \right)^{1/2} = (\det C)^{1/2},$$

$$(2.17c) \qquad c\text{E-criterion} \quad \psi_E(C) = \max_{\ell=1,2}\{\lambda_\ell\}.$$

These criteria can be related to various geometric quantities associated with approximate confidence ellipsoids in the parameter plane; see, for instance, [9, section 2.2]. While the eigenvectors of C represent the orientation of the semiaxes of the ellipsoid, the square root of the eigenvalues λ_ℓ, multiplied with $\left[\Phi_{\chi_2^2}^{-1}(\alpha)\right]^{1/2}$, yield the length of the corresponding semiaxis. Here $\alpha \in (0,1)$ is a given confidence level and $\Phi_{\chi_2^2}$ denotes the cumulative distribution function (CDF) of the χ^2 distribution with two degrees of freedom. We are going to use, exemplarily, the A-criterion as our optimization criterion in what follows, which is proportional to the sum of the eigenvalues and thus to the average squared length of the semiaxes.

We will also be interested in the precision of the estimation of *only one of the two parameters* and we distinguish two cases:

1. When we need to estimate only the ℓth parameter, while the other one is given, we replace the full Jacobian J by its ℓth column. Consequently, the covariance matrix becomes scalar, the confidence ellipsoid reduces to an interval, and all criteria in (2.17) become equivalent. They can be best expressed in terms of the diagonal entry $F_{\ell,\ell}$ of the full Fisher information matrix (2.15).

2. When both parameters are unknown and need to be estimated from the available measurements, but we are only interested in the precision of the ℓth parameter, then the quantity of interest becomes $C_{\ell,\ell}$, i.e., the diagonal entry of the full covariance matrix (2.16).

In either case, the precision of the estimation of the single relevant parameter can be expressed in terms of its (marginal) confidence interval. The radius of this interval for the ℓth parameter is given by

$$(2.18a) \qquad \mathrm{CI}_\ell = \left[\Phi_{\chi_1^2}^{-1}(\alpha)\right]^{1/2} \left[F_{\ell,\ell}\right]^{-1/2} \quad \text{in case 1,}$$

$$(2.18b) \qquad \mathrm{CI}_\ell = \left[\Phi_{\chi_1^2}^{-1}(\alpha)\right]^{1/2} \left[C_{\ell,\ell}\right]^{1/2} \quad \text{in case 2,}$$

where $\Phi_{\chi_1^2}$ denotes the CDF of the χ^2 distribution with one degree of freedom.

3. Optimum experimental design by shape optimization. In this section we come to the main contributions of this paper. The main and novel idea is to use the geometry of the specimen as an experimental design variable in order to increase the accuracy in the estimation of the elastic parameters. In other words, one tries

to maximize the gain of information obtained through an experiment, measured in terms of one of the criteria (2.17); we focus here on the A-criterion. This leads to a novel type of an OED problem, which is addressed by shape optimization techniques.

In a typical setup one employs the parameter identification process and the design of the subsequent experiment in an alternating fashion known as *sequential design*; see, for instance [15]. During an OED phase, the current parameter set $\boldsymbol{p}$ is either considered fixed at its last known value, or one deems it uncertain and uses a robust optimization framework as, for instance, in [16]. Since our concern here is to use the shape of the specimen as a novel type of experimental condition, we concentrate on the design problem only and consider the value of the elastic parameters $\boldsymbol{p}$ fixed.

Our notation concerning the shape optimization mainly follows [27]. Perturbations Ω_t of an initial shape $\Omega \subset \mathbb{R}^2$ will be expressed in terms of a sufficiently smooth vector field $\boldsymbol{V} : \mathbb{R}^2 \to \mathbb{R}^2$. We use the perturbation of identity approach, which maps the points $\boldsymbol{x}_0 \in \Omega$ onto $\Omega_t = T_t(\Omega)$ according to

$$(3.1) \qquad \boldsymbol{x}(t) := T_t(\boldsymbol{x}_0) := \boldsymbol{x}_0 + t\,\boldsymbol{V}(\boldsymbol{x}_0)$$

for $t \geq 0$. Note that $T_0 = \mathrm{id}$ (the identity) and $\Omega_0 = \Omega$ hold.

The outline of our proposed approach is as follows. First we set up the shape optimization problem whose objective expresses the desire to increase the accuracy of the estimation of the elastic parameters. We use the A-criterion (2.17a) based on the covariance matrix C from (2.16) for this purpose, but other criteria can be used as well. Since the covariance matrix depends on the Jacobian of the residuals, which involves the solution of the sensitivity equation, a classical approach based on the chain rule suggests that we have to find the (material) derivative of the solution of the sensitivity equation (2.12) w.r.t. the perturbation vector field $\boldsymbol{V}$. This is, however, quite involved due to the state $\boldsymbol{u}$ appearing in the right-hand side of (2.12), and not covered by standard shape differentiation results in elasticity; see [27, Chapter 3.5] and [8]. Therefore, and also in the interest of reduced regularity requirements, we resort to the material derivative-free approach developed by [29, 18], which leads directly to an adjoint-based representation of the Eulerian derivative of our objective (3.2).

3.1. Shape optimization problem. Let us begin by fixing some notation. We denote from now on the Jacobian of the residuals (2.14) by $J(\Omega; \delta\boldsymbol{u})$ to emphasize the dependence on the geometry Ω of the specimen as well as the dependence on the displacement sensitivities $\delta\boldsymbol{u} = (\delta\boldsymbol{u}_1, \delta\boldsymbol{u}_2)$. On the other hand, we suppress the dependence on the parameter vector since we consider $\boldsymbol{p}$ fixed.

The OED shape optimization problem can be formulated as follows:

$$(3.2) \qquad \text{Minimize} \quad \Psi(\Omega) := \psi_A\left(C(J(\Omega; \delta\boldsymbol{u}))\right),$$

$$(3.3) \qquad \text{where} \quad C(J) := (J^\top \Sigma^{-1} J)^{-1} \quad \text{and} \quad \psi_A(C) := \frac{1}{2}\,\mathrm{trace}\,C$$

hold according to (2.16) and (2.17a). Admissible shapes are those attained from an initial configuration Ω_0 by the perturbation of identity approach, via admissible perturbation fields $\boldsymbol{V}$ according to the following assumption.

ASSUMPTION 3.1. *Admissible velocity fields $\boldsymbol{V}$ satisfy $\boldsymbol{V} = \boldsymbol{0}$ on $\Gamma_D \cup \Gamma_N$.*

This condition ensures that that the clamping part Γ_D as well as the Neumann boundary Γ_N on which forces $\boldsymbol{g}$ are applied are not subject to shape optimization; see Figure 2. The reason for this is that the specimen geometry needs to remain compatible

with the equipment on which the experiment is conducted. By contrast, the traction-free part Γ_{free} of the boundary will be free to move, along with the interior of the domain Ω. The situation concerning the measurement regions R_k deserves particular mention. By design, they are going to remain fixed relative to the clamping and forcing boundaries $\Gamma_D \cup \Gamma_N$. However the material points in the domain Ω "underneath" these regions are free to move.

In order to characterize the Eulerian derivative $\mathrm{d}\Psi(\Omega)[\boldsymbol{V}]$ in the direction of a given perturbation field $\boldsymbol{V}$ we introduce the Lagrangian associated with (3.2) on the perturbed domain $\Omega_t = T_t(\Omega)$ (see (3.1)) as follows:

$$(3.4) \quad \mathcal{L}_t(t, \boldsymbol{u}_t, \delta\boldsymbol{u}_{1,t}, \delta\boldsymbol{u}_{2,t}, \boldsymbol{z}_t, \boldsymbol{w}_{1,t}, \boldsymbol{w}_{2,t})$$
$$= \frac{1}{2} \operatorname{trace} \left(J(\Omega_t; \delta\boldsymbol{u}_t)^\top \Sigma^{-1} J(\Omega_t; \delta\boldsymbol{u}_t) \right)^{-1} + \int_{\Omega_t} \boldsymbol{\varepsilon}(\boldsymbol{z}_t) : \mathbb{C}\,\boldsymbol{\varepsilon}(\boldsymbol{u}_t)\,\mathrm{d}\boldsymbol{x}$$
$$- \int_{\Gamma_{N,t}} \boldsymbol{g} \cdot \boldsymbol{z}_t\,\mathrm{d}\boldsymbol{s} + \sum_{\ell=1}^2 \int_{\Omega_t} \boldsymbol{\varepsilon}(\boldsymbol{w}_{\ell,t}) : \mathbb{C}\,\boldsymbol{\varepsilon}(\delta\boldsymbol{u}_{\ell,t})\,\mathrm{d}\boldsymbol{x} + \sum_{\ell=1}^2 \int_{\Omega_t} \boldsymbol{\varepsilon}(\boldsymbol{w}_{\ell,t}) : \mathbb{C}_\ell\,\boldsymbol{\varepsilon}(\boldsymbol{u}_t)\,\mathrm{d}\boldsymbol{x}.$$

The Jacobian on the perturbed domain is defined as

$$(3.5) \qquad \left[J(\Omega_t; \delta\boldsymbol{u}_t)_{k,\ell} \right] = \frac{1}{|R_k|} \int_{R_k} \delta\boldsymbol{u}_{\ell,t} \cdot \boldsymbol{e}_k\,\mathrm{d}\boldsymbol{x}, \quad k = 1, \ldots, n_{\text{meas}},\ \ell = 1, 2;$$

compare (2.14). It expresses the fact that the measurement regions will remain independent of the perturbation field.

The second and third lines in (3.4) denote the weak formulations of the elasticity and sensitivity equations (2.4) and (2.12) on the perturbed domain Ω_t, respectively. The adjoint equations governing the *adjoint states* $\boldsymbol{z}_t$ and $\boldsymbol{w}_{\ell,t}$, $\ell = 1, 2$, can be derived, as usual, by differentiating (3.4) w.r.t. the forward and sensitivity state variables $\boldsymbol{u}_t$ and $\delta\boldsymbol{u}_{\ell,t}$, respectively. As seen below, the adjoint states will only be needed in the unperturbed domain ($t = 0$) and therefore will be stated later.

The next step is to pull the Lagrangian back to the unperturbed domain via the substitution rule for integrals. The pulled-back states and adjoint states are defined as $\boldsymbol{u}^t := \boldsymbol{u}_t \circ T_t$ etc. Using the abbreviations

$$\gamma_t = \det(DT_t), \qquad \omega_t = \det(DT_t)\,\|(DT_t)^{-\top}\,\boldsymbol{n}\|,$$

we obtain the family of pulled-back Lagrangians

$$(3.6) \quad \mathcal{L}^t(t, \boldsymbol{u}^t, \delta\boldsymbol{u}_1^t, \delta\boldsymbol{u}_2^t, \boldsymbol{z}^t, \boldsymbol{w}_1^t, \boldsymbol{w}_2^t) = \frac{1}{2}\operatorname{trace}\left(J^t(\Omega; \delta\boldsymbol{u}^t)^\top \Sigma^{-1} J^t(\Omega; \delta\boldsymbol{u}^t) \right)^{-1}$$
$$+ \int_\Omega \boldsymbol{\varepsilon}^t(\boldsymbol{z}^t) : \mathbb{C}\,\boldsymbol{\varepsilon}^t(\boldsymbol{u}^t)\,\gamma_t\,\mathrm{d}\boldsymbol{x} - \int_{\Gamma_N} \boldsymbol{g}^t \cdot \boldsymbol{z}^t\,\omega_t\,\mathrm{d}\boldsymbol{s}$$
$$+ \sum_{\ell=1}^2 \int_\Omega \boldsymbol{\varepsilon}^t(\boldsymbol{w}_\ell^t) : \mathbb{C}\,\boldsymbol{\varepsilon}^t(\delta\boldsymbol{u}_\ell^t)\,\gamma_t\,\mathrm{d}\boldsymbol{x} + \sum_{\ell=1}^2 \int_\Omega \boldsymbol{\varepsilon}^t(\boldsymbol{w}_\ell^t) : \mathbb{C}_\ell\,\boldsymbol{\varepsilon}^t(\boldsymbol{u}^t)\,\gamma_t\,\mathrm{d}\boldsymbol{x}.$$

The transformed differential operator

$$(3.7) \qquad \boldsymbol{\varepsilon}^t(\boldsymbol{u}^t)(\boldsymbol{x}) = \frac{1}{2}\left[(D\boldsymbol{u}^t)(\boldsymbol{x})(DT_t)^{-1}(\boldsymbol{x}) + (DT_t)^{-\top}(\boldsymbol{x})\,(D\boldsymbol{u}^t)(\boldsymbol{x})^\top \right]$$

is obtained using the chain rule; see [27, equation (3.139)]. The boundary traction on Γ_N is simply defined by $\boldsymbol{g}^t(\boldsymbol{x}) = \boldsymbol{g}(T_t(\boldsymbol{x})) = \boldsymbol{g}(\boldsymbol{x})$, where the last equality is

due to Assumption 3.1. Finally, the transformed Jacobian $J^t(\Omega; \delta u^t)$ of the residuals obtained from (3.5) has entries of the form

$$(3.8) \qquad [J^t(\Omega; \delta u^t)]_{k,\ell} = \frac{1}{|R_k|} \int_{T_t^{-1}(R_k)} \delta u_\ell^t \cdot e_k \, \gamma_t \, \mathrm{d}x,$$

where, as before, $k = 1, \ldots, n_{\mathrm{meas}}$ denotes the measurement index and $\ell = 1, 2$ selects the parameter.

Following [29, 18], we obtain the Eulerian derivative $\mathrm{d}\Psi(\Omega)[V]$ as the *partial* derivative of $\mathcal{L}^t$, evaluated at $t = 0$. In other words,

$$(3.9) \qquad \mathrm{d}\Psi(\Omega)[V] = \frac{\partial}{\partial t} \mathcal{L}^t(0, u, \delta u_1, \delta u_2, z, w_1, w_2)$$

holds, where u, δu_1, and δu_2 are the solutions of the forward and sensitivity problems (2.4) and (2.12), respectively. The computation of material derivatives of the state variables is thus avoided.

The adjoint states z, w_1, and w_2 are the solutions to suitably defined adjoint equations. For their definition we introduce the following abbreviations. The $n_{\mathrm{meas}} \times 2$-matrix G is defined as

$$(3.10) \qquad G := -\Sigma^{-1} J(\Omega; \delta u) \, C(J(\Omega; \delta u))^2,$$

and g_1, g_2 are its columns. Moreover, we denote by $j_1(\Omega; \delta u_1)$ and $j_2(\Omega; \delta u_2)$ the columns of the Jacobian $J(\Omega; \delta u)$, where $\delta u = (\delta u_1, \delta u_2)$. Notice that j_1 depends only on δu_1 and j_2 depends only on δu_2; see (3.5). Differentiating (3.6) at $t = 0$ w.r.t. u and δu_ℓ ($\ell = 1, 2$), respectively, we obtain the following equations for the adjoint states.

PROPOSITION 3.2. *The adjoint states z and w_ℓ ($\ell = 1, 2$) are defined as the unique solutions in $\mathcal{V}$ of*

$$(3.11) \qquad \int_\Omega \varepsilon(z) : \mathbb{C} \, \varepsilon(v) \, \mathrm{d}x + \sum_{\ell=1}^2 \int_\Omega \varepsilon(w_\ell) : \mathbb{C}_\ell \varepsilon(v) \, \mathrm{d}x = 0 \quad \textit{for all } v \in \mathcal{V}$$

and

$$(3.12) \qquad \int_\Omega \varepsilon(w_\ell) : \mathbb{C} \, \varepsilon(v) \, \mathrm{d}x + g_\ell \cdot j_\ell(\Omega; v) = 0 \quad \textit{for all } v \in \mathcal{V},$$

respectively.

Proof. Equation (3.11) for the adjoint state z is obtained in a straightforward way, by differentiation of the pulled-back Lagrangian (3.6) at $t = 0$ w.r.t. u, and then setting the directional derivative in the direction of an arbitrary element $v \in \mathcal{V}$ equal to zero. The pair of adjoint equations (3.12) is obtained similarly, but by differentiation w.r.t. δu_ℓ. Only the first term in (3.6) at $t = 0$,

$$(3.13) \qquad \frac{1}{2} \mathrm{trace} \left(J(\Omega; \delta u)^\top \Sigma^{-1} J(\Omega; \delta u) \right)^{-1} = \frac{1}{2} \mathrm{trace} \, C \left(J(\Omega; \delta u) \right),$$

deserves a closer look. Recall that $C(\cdot)$ was defined in (3.3). Elementary calculations show that C is Fréchet differentiable, provided that J has full column rank, and that its directional derivatives are given by

$$(3.14) \qquad \frac{\mathrm{d}}{\mathrm{d}J} C(J) \, \delta J = -C(J) \left[J^\top \Sigma^{-1} \delta J + \delta J^\top \Sigma^{-1} J \right] C(J).$$

The chain rule, together with $\operatorname{trace}(A) = \operatorname{trace}(A^\top)$ and the symmetry of Σ and $C(J)$ as well as $\operatorname{trace}(A\,B\,C) = \operatorname{trace}(C\,A\,B)$ for matrices of suitable size, yields the following expression for the directional derivative of (3.13) w.r.t. $\delta\boldsymbol{u}_\ell$ in the direction of $\boldsymbol{v}$:

$$\frac{\partial}{\partial\,\delta\boldsymbol{u}_\ell}\left[\frac{1}{2}\operatorname{trace} C\left(J(\Omega;\delta\boldsymbol{u})\right)\right]\boldsymbol{v}$$

$$= -\operatorname{trace}\left(C(J(\Omega;\delta\boldsymbol{u}))\,J(\Omega;\delta\boldsymbol{u})^\top\Sigma^{-1}\left[\frac{\partial}{\partial\,\delta\boldsymbol{u}_\ell}J(\Omega;\delta\boldsymbol{u})\,\boldsymbol{v}\right]C(J(\Omega;\delta\boldsymbol{u}))\right)$$

$$= -\operatorname{trace}\left(C(J(\Omega;\delta\boldsymbol{u}))^2\,J(\Omega;\delta\boldsymbol{u})^\top\Sigma^{-1}\left[\frac{\partial}{\partial\,\delta\boldsymbol{u}_\ell}J(\Omega;\delta\boldsymbol{u})\,\boldsymbol{v}\right]\right)$$

$$(3.15)\qquad = G : \left[\frac{\partial}{\partial\,\delta\boldsymbol{u}_\ell}J(\Omega;\delta\boldsymbol{u})\,\boldsymbol{v}\right],$$

where G was defined in (3.10). Using the specific form of the Jacobian (see (2.14) or (3.8) with $t = 0$) we infer that

$$\frac{\partial}{\partial\,\delta\boldsymbol{u}_\ell}\left[J(\Omega;\delta\boldsymbol{u})\,\boldsymbol{v}\right]_{k,m} = \frac{\partial}{\partial\,\delta\boldsymbol{u}_\ell}\left[\frac{1}{|R_k|}\int_{R_k}\delta\boldsymbol{u}_m\cdot\boldsymbol{e}_k\,\mathrm{d}\boldsymbol{x}\right]\boldsymbol{v} = \frac{\delta_{\ell,m}}{|R_k|}\int_{R_k}\boldsymbol{v}\cdot\boldsymbol{e}_k\,\mathrm{d}\boldsymbol{x}$$

holds, where $\delta_{\ell,m}$ is the Kronecker symbol. Consequently, (3.15) becomes

$$\frac{\partial}{\partial\,\delta\boldsymbol{u}_\ell}\left[\frac{1}{2}\operatorname{trace} C\left(J(\Omega;\delta\boldsymbol{u})\right)\right]\boldsymbol{v} = G : \left[\frac{\partial}{\partial\,\delta\boldsymbol{u}_\ell}J(\Omega;\delta\boldsymbol{u})\,\boldsymbol{v}\right] = g_\ell\cdot j_\ell(\Omega;\boldsymbol{v}).$$

This concludes the proof of (3.12). $\qquad\qquad\qquad\qquad\qquad\qquad\qquad\Box$

We are now in the position to formulate our main theorem, which provides a formula for efficient evaluations of the Eulerian derivative of the OED objective Ψ.

THEOREM 3.3. *Suppose that $\boldsymbol{u}$, $\delta\boldsymbol{u}_1$, and $\delta\boldsymbol{u}_2$ are the solutions of the forward and sensitivity problems (2.4) and (2.12) on the domain Ω. Moreover, let $\boldsymbol{z}$, $\boldsymbol{w}_1$, and $\boldsymbol{w}_2$ denote the solutions to the adjoint equations (3.11) and (3.12), respectively. Let $\boldsymbol{V}$ denote a perturbation field satisfying Assumption 3.1. Then the Eulerian derivative of Ψ in the direction of $\boldsymbol{V}$ is given by*

$$\mathrm{d}\Psi(\Omega)[\boldsymbol{V}]$$

$$= G : \frac{1}{|R_k|}\left[\int_{R_k}\nabla\left(\delta\boldsymbol{u}_\ell\cdot\boldsymbol{e}_k\right)\cdot\boldsymbol{V}\,\mathrm{d}\boldsymbol{x}\right]_{k=1,\ldots,n_{meas},\ \ell=1,2}$$

$$- \int_\Omega\operatorname{sym}(D\boldsymbol{z}D\boldsymbol{V}):\mathbb{C}\,\boldsymbol{\varepsilon}(\boldsymbol{u})\,\mathrm{d}\boldsymbol{x} - \int_\Omega\boldsymbol{\varepsilon}(\boldsymbol{z}):\mathbb{C}\,\operatorname{sym}(D\boldsymbol{u}D\boldsymbol{V})\,\mathrm{d}\boldsymbol{x}$$

$$+ \int_\Omega\boldsymbol{\varepsilon}(\boldsymbol{z}):\mathbb{C}\,\boldsymbol{\varepsilon}(\boldsymbol{u})\,\operatorname{div}\boldsymbol{V}\,\mathrm{d}\boldsymbol{x}$$

$$- \int_{\Gamma_N}\boldsymbol{g}\cdot\boldsymbol{z}\left(\operatorname{div}\boldsymbol{V} - \boldsymbol{n}^\top\operatorname{sym}(D\boldsymbol{V})\,\boldsymbol{n}\right)\mathrm{d}\boldsymbol{s}$$

$$- \sum_{\ell=1}^{2}\int_\Omega\operatorname{sym}(D\boldsymbol{w}_\ell D\boldsymbol{V}):\mathbb{C}\,\boldsymbol{\varepsilon}(\delta\boldsymbol{u}_\ell)\,\mathrm{d}\boldsymbol{x} - \sum_{\ell=1}^{2}\int_\Omega\boldsymbol{\varepsilon}(\boldsymbol{w}_\ell):\mathbb{C}\,\operatorname{sym}(D\delta\boldsymbol{u}_\ell D\boldsymbol{V})\,\mathrm{d}\boldsymbol{x}$$

$$+ \sum_{\ell=1}^{2}\int_\Omega\boldsymbol{\varepsilon}(\boldsymbol{w}_\ell):\mathbb{C}\,\boldsymbol{\varepsilon}(\delta\boldsymbol{u}_\ell)\,\operatorname{div}\boldsymbol{V}\,\mathrm{d}\boldsymbol{x}$$

$$-\sum_{\ell=1}^{2}\int_{\Omega}\mathrm{sym}(D\boldsymbol{w}_{\ell}D\boldsymbol{V}):\mathbb{C}_{\ell}\,\boldsymbol{\varepsilon}(\boldsymbol{u})\,\mathrm{d}\boldsymbol{x}-\sum_{\ell=1}^{2}\int_{\Omega}\boldsymbol{\varepsilon}(\boldsymbol{w}_{\ell}):\mathbb{C}_{\ell}\,\mathrm{sym}(D\boldsymbol{u}D\boldsymbol{V})\,\mathrm{d}\boldsymbol{x}$$

(3.16)
$$+\sum_{\ell=1}^{2}\int_{\Omega}\boldsymbol{\varepsilon}(\boldsymbol{w}_{\ell}):\mathbb{C}_{\ell}\,\boldsymbol{\varepsilon}(\boldsymbol{u})\,\mathrm{div}\,\boldsymbol{V}\,\mathrm{d}\boldsymbol{x}.$$

Notice that sym (denoting the symmetric part of a matrix) could be omitted in each and every occurence since $A:\mathbb{C}\,B=B:\mathbb{C}\,A=\mathrm{sym}(B):\mathbb{C}\,A$ holds whenever A is symmetric. The same formula holds with $\mathbb{C}_{\ell}$ in place of $\mathbb{C}$.

Proof. According to (3.9), we need to find the partial derative of (3.6) w.r.t. t, at $t=0$. Collecting terms, we have to differentiate all expressions involving J^{t}, $\boldsymbol{\varepsilon}^{t}$, γ_{t}, ω_{t}, and $\boldsymbol{g}^{t}$. Differentiation of the pull-backs $\boldsymbol{\varepsilon}^{t}$ and $\boldsymbol{g}^{t}$ is standard:

$$\frac{\partial}{\partial t}\boldsymbol{\varepsilon}^{t}(\boldsymbol{u}^{t})\big|_{t=0}=-\frac{1}{2}\left[D\boldsymbol{u}D\boldsymbol{V}+D\boldsymbol{V}^{\top}D\boldsymbol{u}^{\top}\right]=-\,\mathrm{sym}\,(D\boldsymbol{u}D\boldsymbol{V}),$$
$$\frac{\partial}{\partial t}\boldsymbol{g}^{t}\big|_{t=0}=(D\boldsymbol{g})\,\boldsymbol{V};$$

see, for instance, [27, equation (3.142) and Proposition 2.33]. Due to Assumption 3.1, we have $(D\boldsymbol{g})\,\boldsymbol{V}=0$. The derivatives of γ_{t} and ω_{t} can be found in [27, Lemmas 2.31 and 2.49]:

$$\frac{\partial}{\partial t}\gamma_{t}\big|_{t=0}=\mathrm{div}\,\boldsymbol{V},\qquad\frac{\partial}{\partial t}\omega_{t}\big|_{t=0}=\mathrm{div}\,\boldsymbol{V}-\boldsymbol{n}^{\top}(D\boldsymbol{V})\,\boldsymbol{n}=\mathrm{div}\,\boldsymbol{V}-\boldsymbol{n}^{\top}\mathrm{sym}(D\boldsymbol{V})\,\boldsymbol{n}.$$

With these relations, the derivatives of all but the first term in (3.6) can be formulated, yielding the corresponding terms in (3.16).

It remains to differentiate the pulled-back objective $\frac{1}{2}\,\mathrm{trace}\,C(J^{t}(\Omega;\delta\boldsymbol{u}^{t}))$, where $C(\cdot)$ was defined in (3.3). Proceeding as in the proof of Proposition 3.2, we can find

(3.17)
$$\frac{\partial}{\partial t}\frac{1}{2}\,\mathrm{trace}\,C\left(J^{t}(\Omega;\delta\boldsymbol{u}^{t})\right)\big|_{t=0}=G:\frac{\partial}{\partial t}\left[J^{t}(\Omega;\delta\boldsymbol{u}^{t})\right]_{t=0}$$

with G from (3.10). It remains to evaluate the derivative of J^{t}. We address a single component of this expression (see (3.8)):

$$\left[\frac{\partial}{\partial t}J_{k,\ell}^{t}(\Omega;\delta\boldsymbol{u}^{t})\right]_{t=0}=\frac{\partial}{\partial t}\left[\frac{1}{|R_{k}|}\int_{T_{t}^{-1}(R_{k})}\delta\boldsymbol{u}_{\ell}^{t}\cdot\boldsymbol{e}_{k}\,\gamma_{t}\,\mathrm{d}\boldsymbol{x}\right]_{t=0}$$
$$=\frac{1}{|R_{k}|}\left[\int_{R_{k}}\delta\boldsymbol{u}_{\ell}\cdot\boldsymbol{e}_{k}\,\mathrm{div}\,\boldsymbol{V}\,\mathrm{d}\boldsymbol{x}-\int_{\partial R_{k}}\delta\boldsymbol{u}_{\ell}\cdot\boldsymbol{e}_{k}\,(\boldsymbol{V}\cdot\boldsymbol{n})\,\mathrm{d}\boldsymbol{s}\right]$$
$$=\frac{1}{|R_{k}|}\left[\int_{R_{k}}\nabla\,(\delta\boldsymbol{u}_{\ell}\cdot\boldsymbol{e}_{k})\cdot\boldsymbol{V}\,\mathrm{d}\boldsymbol{x}\right].$$

The second equality above follows from $\frac{\partial}{\partial t}\gamma_{t}\big|_{t=0}=\mathrm{div}\,\boldsymbol{V}$ and [27, Proposition 2.46]. Notice that we are using the inverse transformation T_{t}^{-1} here, and therefore the sign of $\boldsymbol{V}$ changes compared to [27, equation (2.114)]. The third equality is a consequence of the divergence theorem. Plugging this derivative into (3.17) concludes the proof. □

For convenience Table 1 summarizes all quantities required for the evaluation of the Eulerian derivative (3.16) of the OED objective. An evaluation of the Jacobian, as needed for efficient least-squares estimation procedures on a given domain Ω as well as

TABLE 1
Quantities required to evaluate the Jacobian (left) of the residuals in the parameter identification problem, and the Eulerian derivatives (right) of the objective in the OED shape optimization problem. The index $\ell = 1, 2$ refers to the parameters to be identified.

Evaluation of the Jacobian J (2.14) in the parameter identification problem			Evaluation of $\mathrm{d}\Psi(\Omega)[\boldsymbol{V}]$ (3.16) in the OED problem		
Quantity	Defined by	Depends on	Quantity	Defined by	Depends on
$\boldsymbol{u}$	(2.4)	—	$\boldsymbol{w}_\ell$	(3.12)	$\boldsymbol{u}$, $\delta\boldsymbol{u}$ (via G)
$\delta\boldsymbol{u}_\ell$	(2.12)	$\boldsymbol{u}$	$\boldsymbol{z}$	(3.11)	$\boldsymbol{w}_\ell$

for the evaluation of the OED objective, requires three elasticity solves. Three more elasticity solves for the adjoint states are needed to evaluate the Eulerian derivative in arbitrary directions $\boldsymbol{V}$.

We remark that the linear elasticity model does not distinguish between tensile and compression experiments. When $\boldsymbol{g}$ is replaced by $-\boldsymbol{g}$ in (2.2a), the solutions $\boldsymbol{u}$ and $\delta\boldsymbol{u}_\ell$ change in sign due to the linearity of the forward and sensitivity problems (2.4) and (2.12). Consequently the Jacobian (2.14) changes sign but the covariance matrix $C(\boldsymbol{p})$ in (2.16) remains the same.

3.2. Shape gradient representations. The Eulerian derivative (3.16) constitutes a linear functional on the space of admissible velocity fields $\boldsymbol{V}$. By the Hadamard structure theorem the Eulerian derivative can likewise be represented by a distribution concentrated on the boundary Γ of the domain Ω, which is applied to the normal vector field $(\boldsymbol{V} \cdot \boldsymbol{n})_{|\Gamma}$ restricted to the boundary; see [27, Theorem 2.27]. Indeed, by tedious calculations involving the divergence theorem, one can obtain the representation

$$\mathrm{d}\Psi(\Omega)[\boldsymbol{V}] = \int_{\Gamma_{\mathrm{free}}} h\,(\boldsymbol{V} \cdot \boldsymbol{n})\,\mathrm{d}\boldsymbol{s},$$

where the so-called Hadamard shape gradient h is given by

$$h = \int_{\Gamma_{\mathrm{free}}} \left[\{-(D\boldsymbol{\sigma})[\boldsymbol{n}]\,\boldsymbol{n} - \mathrm{div}_\Gamma\,\boldsymbol{\sigma}\} \cdot \boldsymbol{z} - \boldsymbol{\sigma}_\Gamma : (D\boldsymbol{z})\right](\boldsymbol{V} \cdot \boldsymbol{n})\,\mathrm{d}\boldsymbol{s}$$

$$+ \sum_{\ell=1}^{2} \int_{\Gamma_{\mathrm{free}}} \left[\{-(D\boldsymbol{\tau}_\ell)[\boldsymbol{n}]\,\boldsymbol{n} - \mathrm{div}_\Gamma\,\boldsymbol{\tau}_\ell\} \cdot \delta\boldsymbol{u}_\ell - (\boldsymbol{\tau}_\ell)_\Gamma : (D\delta\boldsymbol{u}_\ell)\right](\boldsymbol{V} \cdot \boldsymbol{n})\,\mathrm{d}\boldsymbol{s}$$

$$(3.18) \qquad + \sum_{\ell=1}^{2} \int_{\Gamma_{\mathrm{free}}} \boldsymbol{\varepsilon}(\boldsymbol{w}_\ell) : \mathbb{C}_\ell\,\boldsymbol{\varepsilon}(\boldsymbol{u})\,(\boldsymbol{V} \cdot \boldsymbol{n})\,\mathrm{d}\boldsymbol{s}.$$

Here $\boldsymbol{\sigma} = \mathbb{C}\,\boldsymbol{\varepsilon}(\boldsymbol{u})$ and $\boldsymbol{\tau}_\ell := \mathbb{C}\,\boldsymbol{\varepsilon}(\boldsymbol{w}_\ell)$ are the stress fields for the forward and adjoint problems, $\ell = 1, 2$. Moreover, $(D\boldsymbol{\sigma})[\boldsymbol{n}]$ denotes the directional derivative of $\boldsymbol{\sigma}$ in the direction of the outer unit normal vector $\boldsymbol{n}$ on Γ. Furthermore,

$$(3.19) \qquad \boldsymbol{\sigma}_\Gamma := \boldsymbol{\sigma} - (\boldsymbol{\sigma}\,\boldsymbol{n})\,\boldsymbol{n}^\top = \boldsymbol{\sigma}\,(\mathrm{id} - \boldsymbol{n}\,\boldsymbol{n}^\top)$$

is the (rowwise) tangential component of $\boldsymbol{\sigma}$ on Γ, and $\mathrm{div}_\Gamma\,\boldsymbol{\sigma}$ is the (rowwise) tangential divergence of a matrix field $\boldsymbol{\sigma}$ restricted to the boundary, i.e.,

$$(3.20) \qquad \mathrm{div}_\Gamma\,\boldsymbol{\sigma} := \mathrm{div}\,\boldsymbol{\sigma} - (D\boldsymbol{\sigma})[\boldsymbol{n}]\,\boldsymbol{n};$$

see, for instance, [27, Definition 2.52] or [28, equation (8)].

Formula (3.18) is presented here for comparison only, and we will continue to work with (3.16). Notice that (3.18) requires boundary traces of first- and second-order derivatives of the forward and adjoint displacements, while the volume representation (3.16) requires only first-order derivatives in the domain. Hence the argument of [13] applies also here, showing that the volume representation of the Eulerian derivative offers better accuracy in finite element computations.

Following [25], we proceed by calculating the Riesz representer of the linear functional (3.16) w.r.t. an auxiliary linear elasticity inner product. That is, we obtain a displacement field $\boldsymbol{U} \in \mathcal{W} := \{\boldsymbol{U} \in H^1(\Omega; \mathbb{R}^2) : \boldsymbol{U} = \boldsymbol{0} \text{ on } \Gamma_D \cup \Gamma_N\}$ by solving the linear problem

$$(3.21) \qquad \int_\Omega \left[2\,\mu_0\,\boldsymbol{\varepsilon}(\boldsymbol{U}) + \lambda_0\,\text{trace}(\boldsymbol{\varepsilon}(\boldsymbol{U}))\right] : \boldsymbol{\varepsilon}(\boldsymbol{V})\,\mathrm{d}\boldsymbol{x} = \mathrm{d}\Psi(\Omega)[\boldsymbol{V}] \quad \text{for all } \boldsymbol{V} \in \mathcal{W}.$$

The displacement field $\boldsymbol{U}$ then serves as the deformation field in the domain transformation $T_t(\boldsymbol{x}) := \boldsymbol{x} + t\,\boldsymbol{U}(\boldsymbol{x})$ for all $\boldsymbol{x} \in \Omega$, and t will be determined by a line search procedure. The Lamé parameters (λ_0, μ_0) and further details will be specified in section 4.

3.3. Single parameter identification. We return to the discussion at the end of section 2 about the restriction to only one parameter. We distinguish two cases:

1. When we estimate only the ℓth parameter and the other one is known, we replace the Jacobian by its ℓth column, denoted by $j_\ell(\Omega; \delta\boldsymbol{u}_\ell)$. The OED problem (3.2) then reduces to

$$(3.22) \qquad \text{Minimize} \quad \Psi_\ell^{(1)}(\Omega) := \left(j_\ell(\Omega; \delta\boldsymbol{u}_\ell)^\top \Sigma^{-1} j_\ell(\Omega; \delta\boldsymbol{u}_\ell)\right)^{-1}.$$

   Equivalently, we might maximize the ℓth diagonal entry in the Fisher information matrix (2.15). The Eulerian derivative pertaining to (3.22) can be expressed similarly as in (3.16) with changes in the first term, the adjoints $\boldsymbol{w}_\ell$ and $\boldsymbol{z}$, and the sums over ℓ. The first term in (3.16) changes to

$$g_\ell^{(1)} \cdot \frac{1}{|R_k|} \left[\int_{R_k} \nabla\left(\delta\boldsymbol{u}_\ell \cdot \boldsymbol{e}_k\right) \cdot \boldsymbol{V}\,\mathrm{d}\boldsymbol{x}\right]_{k=1,\ldots,n_{\text{meas}}}$$

   with the vector $g_\ell^{(1)}$ defined by

$$g_\ell^{(1)} := -2\,\Sigma^{-1} j_\ell(\Omega; \delta\boldsymbol{u}_\ell)\,C(j_\ell(\Omega; \delta\boldsymbol{u}_\ell))^2.$$

   Notice that $g_\ell^{(1)}$ is *not* identical to the ℓth column of G; compare (3.10). The adjoint states $\boldsymbol{w}_\ell$ and $\boldsymbol{z}$ are obtained as the unique solutions in $\mathcal{V}$ of

$$\int_\Omega \boldsymbol{\varepsilon}(\boldsymbol{z}) : \mathbb{C}\,\boldsymbol{\varepsilon}(\boldsymbol{v})\,\mathrm{d}\boldsymbol{x} + \int_\Omega \boldsymbol{\varepsilon}(\boldsymbol{w}_\ell) : \mathbb{C}_\ell \boldsymbol{\varepsilon}(\boldsymbol{v})\,\mathrm{d}\boldsymbol{x} = 0 \quad \text{for all } \boldsymbol{v} \in \mathcal{V},$$

$$\int_\Omega \boldsymbol{\varepsilon}(\boldsymbol{w}_\ell) : \mathbb{C}\,\boldsymbol{\varepsilon}(\boldsymbol{v})\,\mathrm{d}\boldsymbol{x} + g_\ell^{(1)} \cdot j_\ell(\Omega; \boldsymbol{v}) = 0 \quad \text{for all } \boldsymbol{v} \in \mathcal{V};$$

   compare (3.11) and (3.12). Notice that only one adjoint state of type $\boldsymbol{w}_\ell$ is required.

   Finally, the summation over $\ell = 1, 2$ in (3.16) is omitted.

2. When both parameters are unknown and need to be estimated but we are only interested in the precision of the ℓth parameter, the experimental design

problem (3.2) reduces to

$$(3.23) \qquad \text{Minimize} \quad \Psi_\ell^{(2)}(\Omega) := C(J(\Omega; \delta\boldsymbol{u}))_{\ell,\ell} = \boldsymbol{e}_\ell^\top C(J(\Omega; \delta\boldsymbol{u}))\, \boldsymbol{e}_\ell,$$

where $\boldsymbol{e}_\ell \in \mathbb{R}^2$ is the ℓth unit vector. Straightforward calculations show that the matrix G involved in the first term of (3.16) has to be replaced by

$$G_\ell^{(2)} := -2\,\Sigma^{-1} J(\Omega; \delta\boldsymbol{u})\, C(J(\Omega; \delta\boldsymbol{u}))\, \boldsymbol{e}_\ell\, \boldsymbol{e}_\ell^\top C(J(\Omega; \delta\boldsymbol{u})).$$

Its columns $g_\ell^{(2)}$ appear also in the adjoint equations, which now read

$$\int_\Omega \boldsymbol{\varepsilon}(\boldsymbol{z}) : \mathbb{C}\,\boldsymbol{\varepsilon}(\boldsymbol{v})\, \mathrm{d}\boldsymbol{x} + \sum_{\ell=1}^2 \int_\Omega \boldsymbol{\varepsilon}(\boldsymbol{w}_\ell) : \mathbb{C}_\ell \boldsymbol{\varepsilon}(\boldsymbol{v})\, \mathrm{d}\boldsymbol{x} = 0 \quad \text{for all } \boldsymbol{v} \in \mathcal{V},$$

$$\int_\Omega \boldsymbol{\varepsilon}(\boldsymbol{w}_\ell) : \mathbb{C}\,\boldsymbol{\varepsilon}(\boldsymbol{v})\, \mathrm{d}\boldsymbol{x} + g_\ell^{(2)} \cdot j_\ell(\Omega; \boldsymbol{v}) = 0 \quad \text{for all } \boldsymbol{v} \in \mathcal{V}.$$

In this case the summation over $\ell = 1, 2$ in (3.16) remains.

3.4. Stress and perimeter penalty terms. The OED shape optimization problem (3.2) discussed so far suffers from one apparent flaw. Roughly speaking, for any prescribed value of the boundary stress $\boldsymbol{\sigma n} = \boldsymbol{g}$ on Γ_N, a thinning of the specimen will lead to an increase in displacement values $\boldsymbol{u}$, and thus to a better informed experiment since the sensitivity values $\delta\boldsymbol{u}_\ell$ will increase as well; see (2.12). One possible remedy would be to assume that the measurements' standard deviations σ_k scale with the measurements and thus with the displacement $\boldsymbol{u}$. This amounts to a constant *relative* measurement accuracy and it would lead to an additional dependency of Σ and thus of the estimator covariance matrix $C = (J^\top \Sigma^{-1} J)^{-1}$ and the objective (3.2) on the domain Ω. Since constant *absolute* variance optical measurements are not unrealistic for our setting, we do not pursue this further. By contrast, we will prevent excessive specimen thinning by adding the stress penalty term

$$(3.24) \qquad \mathcal{P}_{\boldsymbol{\sigma}}(\Omega; \boldsymbol{u}) := \int_\Omega \max\{0,\ |\boldsymbol{\sigma}_{\mathrm{ps}}^D|_F - \sigma_{\max}\}^2\, \mathrm{d}\boldsymbol{x}$$

to the objective (3.2). This penalty term becomes active whenever the von Mises stress $|\boldsymbol{\sigma}_{\mathrm{ps}}^D|_F$ exceeds the allowable stress $\sigma_{\max}$. A proper definition of the von Mises stress requires that we consider the 3D analogue $\boldsymbol{\sigma}_{\mathrm{ps}}$ of the planar stress tensor $\boldsymbol{\sigma}$. To define it, we require the 3D analogue of the Lamé coefficients λ and μ in (2.5), which are given by

$$(3.25) \qquad \lambda^{\mathrm{3D}} = \lambda + \frac{\lambda^2}{2\mu - \lambda} \qquad \text{and} \qquad \mu^{\mathrm{3D}} = \mu.$$

Note that the second Lamé coefficient (shear modulus) μ remains the same. Assuming the plane-stress situation (where the specimen can move freely in thickness direction), the corresponding 3D strain and stress tensors are given as follows:

$$\boldsymbol{\varepsilon}_{\mathrm{ps}}(\boldsymbol{u}) := \begin{pmatrix} \boldsymbol{\varepsilon}(\boldsymbol{u}) & \begin{matrix} 0 \\ 0 \end{matrix} \\ 0 \quad 0 & \varepsilon_{33}(\boldsymbol{u}) \end{pmatrix} \quad \text{and} \quad \boldsymbol{\sigma}_{\mathrm{ps}} := \mathbb{C}^{\mathrm{3D}} \boldsymbol{\varepsilon}_{\mathrm{ps}} = \begin{pmatrix} * & * & 0 \\ * & * & 0 \\ 0 & 0 & 0 \end{pmatrix},$$

where $\varepsilon_{33}(\boldsymbol{u}) := -\frac{\lambda^{\mathrm{3D}}\, \mathrm{trace}(\boldsymbol{\varepsilon}(\boldsymbol{u}))}{2\mu + \lambda^{\mathrm{3D}}}$. Equivalently to (2.5), we have

$$(3.26) \qquad \boldsymbol{\sigma}_{\mathrm{ps}} = \mathbb{C}^{\mathrm{3D}} \boldsymbol{\varepsilon}_{\mathrm{ps}} = 2\,\mu\,\boldsymbol{\varepsilon}_{\mathrm{ps}} + \lambda^{\mathrm{3D}}\, \mathrm{trace}(\boldsymbol{\varepsilon}_{\mathrm{ps}})\, \mathrm{id}_{3\times 3},$$

and the positivity requirement $\lambda + \mu > 0$ translates into $3\lambda^{3D} + 2\mu > 0$. Notice that the above formula for ε_{33} is easily obtained by the plane-stress assumption $(\boldsymbol{\sigma}_{\text{ps}})_{33} = 0$. Finally $\boldsymbol{\sigma}_{\text{ps}}^D := \boldsymbol{\sigma}_{\text{ps}} - \frac{1}{3}\operatorname{trace}(\boldsymbol{\sigma}_{\text{ps}})\,\text{id}_{3\times3}$ is the deviatoric component of the 3D plane-stress state and $|\boldsymbol{\sigma}_{\text{ps}}^D|_F$ is its Frobenius norm.

This explains the composition of the stress penalty (3.24). In our experiments, we also added a standard perimeter penalty

$$(3.27) \qquad \mathcal{P}_\Gamma(\Omega) := \int_{\Gamma_{\text{free}}} \mathrm{d}\boldsymbol{s},$$

which helps smooth the boundary and is beneficial with a view toward producibility of the specimen.

In place of (3.2) we consider from now on the more general problem

$$(3.28) \qquad \text{Minimize} \quad \widetilde{\Psi}(\Omega) := \psi_A\left(C(J(\Omega; \delta\boldsymbol{u}))\right) + \alpha_{\boldsymbol{\sigma}}\mathcal{P}_{\boldsymbol{\sigma}}(\Omega; \boldsymbol{u}) + \alpha_\Gamma\mathcal{P}_\Gamma(\Omega),$$

where $\alpha_{\boldsymbol{\sigma}} \geq 0$ and $\alpha_\Gamma \geq 0$ are the penalty parameters. Let us briefly discuss the implications of the two additional terms. On the perturbed domain Ω_t the stress penalty reads

$$\mathcal{P}_{\boldsymbol{\sigma},t}(\Omega_t; \boldsymbol{u}_t) := \int_{\Omega_t} \max\{0,\ |\boldsymbol{\sigma}_{\text{ps},t}^D|_F - \sigma_{\max}\}^2\,\mathrm{d}\boldsymbol{x}.$$

Its pull-back to Ω is

$$(3.29) \qquad \mathcal{P}_{\boldsymbol{\sigma}}^t(\Omega; \boldsymbol{u}) = \int_\Omega \max\{0,\ |\boldsymbol{\sigma}_{\text{ps}}^{D,t}|_F - \sigma_{\max}\}^2\,\gamma_t\,\mathrm{d}\boldsymbol{x},$$

where

$$\boldsymbol{\sigma}_{\text{ps}}^t = \mathbb{C}^{3D}\boldsymbol{\varepsilon}_{\text{ps}}^t(\boldsymbol{u}^t) = \mathbb{C}^{3D}\begin{pmatrix} \boldsymbol{\varepsilon}^t(\boldsymbol{u}^t) & \begin{matrix} 0 \\ 0 \end{matrix} \\ \begin{matrix} 0 & 0 \end{matrix} & -\frac{\lambda^{3D}\operatorname{trace}(\boldsymbol{\varepsilon}^t(\boldsymbol{u}^t))}{2\mu+\lambda^{3D}} \end{pmatrix} \quad \text{and} \quad \boldsymbol{\sigma}_{\text{ps}}^{D,t} = [\boldsymbol{\sigma}_{\text{ps}}^t]^D$$

holds with $\boldsymbol{\varepsilon}^t(\boldsymbol{u}^t)$ from (3.7). The term (3.29) is added to the Lagrangian (3.6). Its differentiation at $t = 0$ w.r.t. $\boldsymbol{u}$ in the direction of $\boldsymbol{v}$ gives us an additional term which appears in the "right-hand side" of the adjoint equation (3.11) for $\boldsymbol{z}$. The latter is thus replaced by

$$(3.30) \quad \int_\Omega \boldsymbol{\varepsilon}(\boldsymbol{z}) : \mathbb{C}\,\boldsymbol{\varepsilon}(\boldsymbol{v})\,\mathrm{d}\boldsymbol{x} + \sum_{\ell=1}^2 \int_\Omega \boldsymbol{\varepsilon}(\boldsymbol{w}_\ell) : \mathbb{C}_\ell \boldsymbol{\varepsilon}(\boldsymbol{v})\,\mathrm{d}\boldsymbol{x}$$

$$+ 2\alpha_{\boldsymbol{\sigma}} \int_\Omega \max\{0,\ |\boldsymbol{\sigma}_{\text{ps}}^D|_F - \sigma_{\max}\}\,\frac{\boldsymbol{\sigma}_{\text{ps}}^D}{|\boldsymbol{\sigma}_{\text{ps}}^D|_F} : \boldsymbol{\sigma}_{\text{ps}}^D\left(\boldsymbol{\varepsilon}(\boldsymbol{v})\right)\,\mathrm{d}\boldsymbol{x} = 0 \quad \text{for all } \boldsymbol{v} \in \mathcal{V}.$$

The adjoints $\boldsymbol{w}_\ell$ ($\ell = 1, 2$) remain unchanged; see (3.12).

We proceed similarly for the perimeter penalty (3.27), whose pull-back is given by

$$(3.31) \qquad \mathcal{P}_\Gamma^t(\Omega) := \int_{\Gamma_{\text{free}}} \omega_t\,\mathrm{d}\boldsymbol{s}.$$

Since it does not depend on state variables, no further changes to the adjoint equations are necessary. By adding the partial derivatives of (3.29) and (3.31) w.r.t. t at $t = 0$ to (3.16) we obtain the Eulerian shape derivative for the penalized problem (3.28) as stated in the following theorem. The details are left to the reader.

THEOREM 3.4. *Suppose that $\boldsymbol{u}$, $\delta\boldsymbol{u}_1$, and $\delta\boldsymbol{u}_2$ are the solutions of the forward and sensitivity problems (2.4) and (2.12) on the domain Ω. Moreover, let $\boldsymbol{z}$, $\boldsymbol{w}_1$, and $\boldsymbol{w}_2$ denote the solutions to the adjoint equations (3.30) and (3.12), respectively. Let $\boldsymbol{V}$ denote a perturbation field satisfying Assumption 3.1. Then the Eulerian derivative of $\widetilde{\Psi}$ in the direction of $\boldsymbol{V}$ is given by*

$$\mathrm{d}\widetilde{\Psi}(\Omega)[\boldsymbol{V}] = formula\ (3.16)$$

$$- 2\,\alpha_{\boldsymbol{\sigma}} \int_{\Omega} \max\{0,\ |\boldsymbol{\sigma}_{ps}^D|_F - \sigma_{\max}\}\,\frac{\boldsymbol{\sigma}_{ps}^D}{|\boldsymbol{\sigma}_{ps}^D|_F} : \boldsymbol{\sigma}_{ps}^D\left(\mathrm{sym}(D\boldsymbol{u}D\boldsymbol{V})\right)\,\mathrm{d}\boldsymbol{x}$$

$$+ \alpha_{\boldsymbol{\sigma}} \int_{\Omega} \max\{0,\ |\boldsymbol{\sigma}_{ps}^D|_F - \sigma_{\max}\}^2\,\mathrm{div}\,\boldsymbol{V}\,\mathrm{d}\boldsymbol{x}$$

$$(3.32) \qquad + \alpha_{\Gamma} \int_{\Gamma_{free}} \left(\mathrm{div}\,\boldsymbol{V} - \boldsymbol{n}^{\top}\,\mathrm{sym}(D\boldsymbol{V})\,\boldsymbol{n}\right)\,\mathrm{d}\boldsymbol{s}.$$

4. Numerical experiments. In this section we describe a number of numerical experiments based on the setup described in Figures 1 and 2. As mentioned earlier, the elasticity parameters will be considered fixed since we are mainly interested in solving the OED problem.

We choose nominal parameters

$$(4.1) \qquad\qquad \lambda = 943\,\mathrm{N/mm}^2, \quad \mu = 803\,\mathrm{N/mm}^2,$$

which corresponds to a certain polycarbonate with elasticity modulus and Poisson ratio $E^{3D} = 2200\,\mathrm{N/mm}^2$ and $\nu^{3D} = 0.37$ or equivalently, Lamé parameters
(4.2)

$$\lambda^{3D} = \frac{E^{3D}\,\nu^{3D}}{(1 + \nu^{3D})(1 - 2\,\nu^{3D})} = 2285\,\mathrm{N/mm}^2, \quad \mu^{3D} = \frac{E^{3D}}{2\,(1 + \nu^{3D})} = 803\,\mathrm{N/mm}^2.$$

The relationship between the 2D and 3D Lamé parameters was described in the transformation formula (3.25). To obtain a consistent set of dimensions, all lengths will be measured in mm. All measurements are assumed to have identical standard deviation $\sigma_k \equiv \sigma = 0.1\,\mathrm{mm}$.

All elasticity problems (see Table 1) were discretized using P_2 (piecewise quadratic, continuous) finite elements on triangular meshes in 2D. Consequently, the stresses such as $\boldsymbol{\sigma} = \mathbb{C}\,\boldsymbol{\varepsilon}(\boldsymbol{u})$ are piecewise linear functions.

In all of our case studies, we consider a symmetric situation with a horizontal symmetry axis $\Gamma_{\mathrm{symmetry}}$, and only the upper half of the domain is involved in the calculations and will be displayed. The boundary conditions along the symmetry axis are $\boldsymbol{e}_1^{\top}\boldsymbol{\sigma}\,\boldsymbol{n} = 0$ and $\boldsymbol{e}_2^{\top}\boldsymbol{u} = 0$, and likewise for the sensitivity and adjoint equations.

All computations were started with an initial configuration of a rectangle of 15 mm width and 150 mm length, i.e., the width of the full specimen is 30 mm. The initial shape with the undeformed mesh and a typical configuration of measurement regions can be seen in Figure 3. Both horizontal and vertical displacements are measured in each region, so that $n_{\mathrm{meas}} = 20$ holds. A constant tensile stress of $\boldsymbol{g} = 220\,\mathrm{N/mm}$ is applied to the right boundary, which amounts to a combined force of 6600 N per
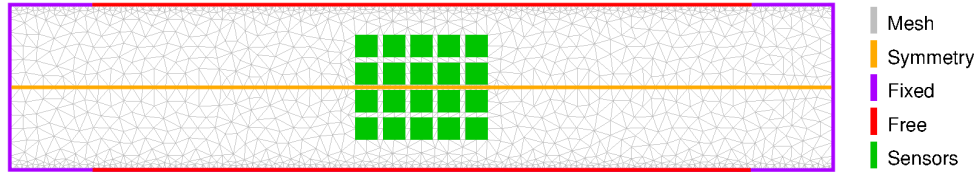
FIG. 3. *Initial shape of the* full *specimen with undeformed mesh, symmetry axis, clamping conditions, free boundary, and configuration of measurement regions (sensors) used.*

mm depth of the specimen. In the initial configuration this results in a maximum horizontal displacement of approximately 1.5 mm.

The computational mesh is created so that it resolves the rectangular measurement domains. In our theory, we allowed the material points underneath the measurement domains to move; cf. (3.5). In numerical practice, we prevent this movement in order to avoid degenerate regions due to uneven mesh movement. Furthermore, the boundary points near Γ_D and Γ_N are also kept fixed. This is, on the one hand, a practical consideration in order to maintain a straight fixation of the specimen in the testing device. On the other hand, stress peaks in the corners of the domain might cause difficulties during the shape optimization procedure. This additional fixed boundary which is exempt from shape optimization is described by

$$\Gamma_{\text{fixed}} := \left\{ \boldsymbol{x} \in \Gamma_{\text{free}} : \text{dist}\left(\boldsymbol{x}, \Gamma_D\right) < \delta \ \text{or} \ \text{dist}\left(\boldsymbol{x}, \Gamma_N < \delta\right) \right\},$$

where δ is chosen as 10% of the sample length and $\text{dist}(\boldsymbol{x}, \mathcal{S})$ denotes the Euclidean distance between a point $\boldsymbol{x}$ and a set $\mathcal{S}$.

Fixing the measurement regions as well as the holding fixture is easily achieved by restricting the deformation space $\mathcal{W}$ for the auxiliary elasticity problem (3.21) to

$$\widetilde{\mathcal{W}} := \{ \boldsymbol{U} \in H^1(\Omega; \mathbb{R}^2) : \boldsymbol{U} = \boldsymbol{0} \ \text{on} \ \Gamma_D \cup \Gamma_N \cup \Gamma_{\text{fixed}} \cup \Gamma_{\text{symmetry}}$$
$$\text{and on} \ \text{cl}\, R_k \ \text{for} \ k = 1, \ldots, n_{\text{meas}} \}.$$

Here $\text{cl}\, R_k$ denotes the closure of R_k. The measurement subdomains as well as the inert boundary $\Gamma_D \cup \Gamma_N \cup \Gamma_{\text{fixed}} \cup \Gamma_{\text{symmetry}}$ are denoted by *Sensors (green)* and *Fixed (violet)* in Figure 3. Taking into account the addition of the two penalty terms of the objective as discussed in subsection 3.4, the auxiliary elasticity problem to obtain the Riesz representer of the Eulerian shape derivative amounts to finding the displacement field $\boldsymbol{U} \in \widetilde{\mathcal{W}}$ such that

$$(4.3) \qquad \int_{\Omega} [2\,\mu_0\,\boldsymbol{\varepsilon}(\boldsymbol{U}) + \lambda_0 \ \text{trace}(\boldsymbol{\varepsilon}(\boldsymbol{U}))] : \boldsymbol{\varepsilon}(\boldsymbol{V})\,\mathrm{d}\boldsymbol{x} = \mathrm{d}\widetilde{\Psi}(\Omega)[\boldsymbol{V}] \quad \text{for all} \ \boldsymbol{V} \in \widetilde{\mathcal{W}}.$$

In our computations we used nonconstant Lamé parameters λ_0 and μ_0. Following [24] these parameters were obtained by first solving the following elliptic problem on the current domain Ω,

$$(4.4a) \qquad \qquad \Delta \mu_0 = 0 \qquad \text{in} \ \Omega,$$

$$(4.4b) \qquad \qquad \mu_0 = \mu_{\text{min}} \quad \text{on} \ \Gamma_{\text{symmetry}},$$

$$(4.4c) \qquad \qquad \mu_0 = \mu_{\text{max}} \quad \text{on} \ \Gamma_{\text{free}},$$

$$(4.4d) \qquad \qquad \frac{\partial \mu_0}{\partial \boldsymbol{n}} = 0 \qquad \text{on} \ \Gamma_{\text{fixed}},$$

FIG. 4. *Lamé parameters λ_0 and μ_0 (in N/mm^2) used in (4.3). The top boundary is Γ_{free}, and the bottom boundary is $\Gamma_{symmetry}$.*

where $\mu_{\min} = 1$ and $\mu_{\max} = 10$. Subsequently the corresponding first Lamé coefficient λ_0 was set according to

$$(4.5) \qquad \lambda_0 = \frac{\nu_{\mathrm{const}}}{0.5 - \nu_{\mathrm{const}}} \, \mu_0$$

with Poisson ratio $\nu_{\mathrm{const}} = 0.45$. This value near the incompressibility threshold of 0.5 ensures small volume changes when the deformation field $\boldsymbol{U}$ is applied to the computational mesh. Moreover mesh transformations obtained with this Lamé coefficients need less remeshing because the boundary nodes at the free boundary tend to remain equally distributed and the largest cell geometry deformations are shifted toward the symmetry boundary, which is not subject to optimization. The resulting functions for λ_0 and μ_0 on the initial geometry are shown in Figure 4.

We followed an optimize-then-discretize approach and implemented a gradient descent method to optimize the specimen shape according to the shape optimization problem (3.2). The deformation field $\boldsymbol{U}$ from (4.3) serves as the descent direction and it generates the transformation $T_t = \mathrm{id} + t\,\boldsymbol{U}$ which is applied to the computational mesh representing the current domain Ω. The parameter $t > 0$ is obtained via an Armijo backtracking line search; see, for instance, [21, Algorithm 3.1]. The trial step size t is accepted if

$$\widetilde{\Psi}(T_t(\Omega)) \leq \widetilde{\Psi}(\Omega) + t\,\sigma\,\mathrm{d}\widetilde{\Psi}(\Omega)[\boldsymbol{U}]$$

holds with $\sigma = 0.01$. When a step is rejected the step size t is reduced to $\beta\,t$ with $\beta = 0.5$. The gradient descent method was stopped as soon as the relative stopping criterion

$$(4.6) \qquad \frac{\widetilde{\Psi}(T_t(\Omega)) - \widetilde{\Psi}(\Omega)}{\widetilde{\Psi}(\Omega)} \leq \epsilon$$

was satisfied.

Our algorithm observes the mesh quality in terms of the aspect ratio (the ratio of the diameters of inscribed and circumscribed circles, times the cell dimension) of every cell. Remeshing is triggered as soon as an element has an aspect ratio lower than 0.1 at the end of a gradient descent step. During remeshing the measurement domains are preserved but additional boundary nodes may be added between existing ones in case boundary nodes become unevenly spaced. Additional boundary nodes are placed based on linear interpolation. The occurence of remeshing will be indicated in the numerical results.

Finally our method monitors the three contributions to the objective (3.28) individually. In the case that the combined penalty terms increase significantly from one iteration to the next, the accepted Armijo step size is reduced as a precaution to avoid irregularities in the free boundary part of the mesh. This typically occurs only in the initial iterations and can be seen at the beginning of the step size plot in Figure 5.
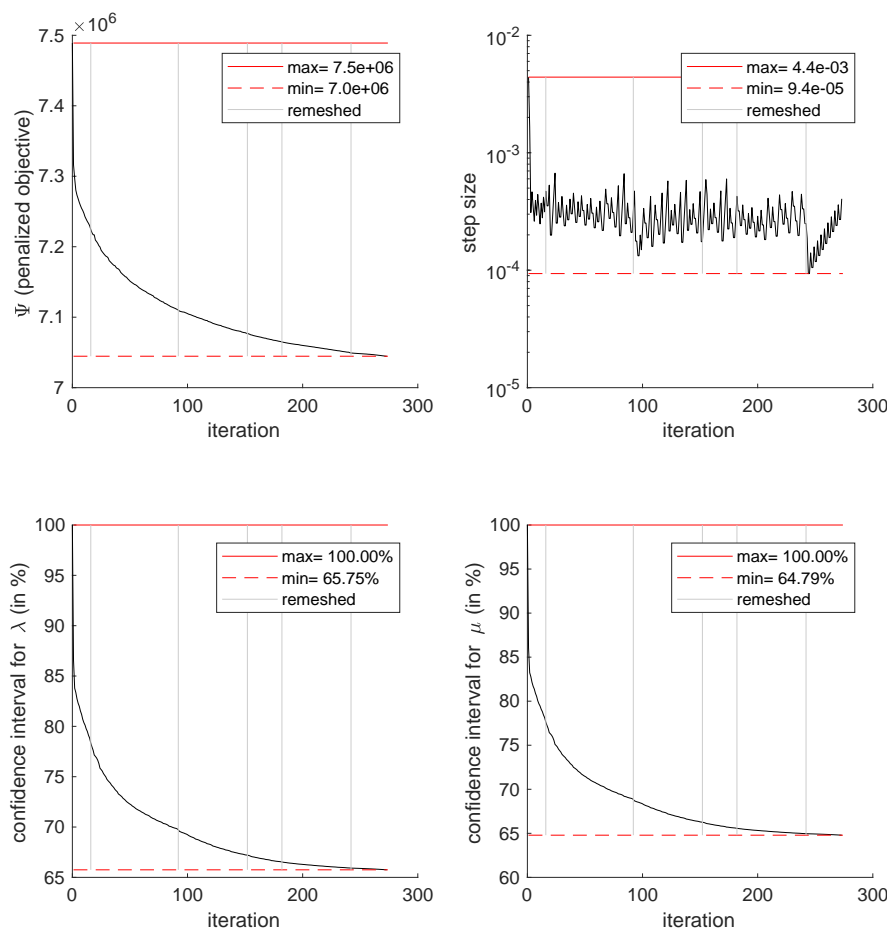
FIG. 5. *Experiment* 1*: evolution of the objective function* $\widetilde{\Psi}$ *including penalty terms, accepted line search step sizes* t*, and relative sizes of the confidence interval for each parameter.*

TABLE 2
Penalty parameters $(\alpha_{\boldsymbol{\sigma}}, \alpha_{\Gamma})$ *and the stopping tolerance* ϵ *used for the case studies in this section.*

Section	Parameters	$\alpha_{\boldsymbol{\sigma}}$	α_{Γ}	ϵ
Subsection 4.1	(λ, μ)	5e1	2e4	1e−5
Subsection 4.2	λ	1e2	5e2	1e−5
Subsection 4.2	μ	5e−2	1e1	1e−5

All computations were implemented in the finite element toolbox FEniCS (version 2017.1); see [20]. In the remainder of this section we describe numerical experiments and results for three different settings. In the first setting (subsection 4.1) we consider the case where both Lamé coefficients (λ, μ) are to be identified. In subsection 4.2 we focus on the two single-parameter cases of type 1 as described in subsection 3.3, i.e., only one of the Lamé parameters needs to be estimated. Table 2 shows the values of the penalty parameters $(\alpha_{\boldsymbol{\sigma}}, \alpha_{\Gamma})$ as well as the tolerance ϵ in the stopping criterion (4.6) which are in effect in each case. The maximal

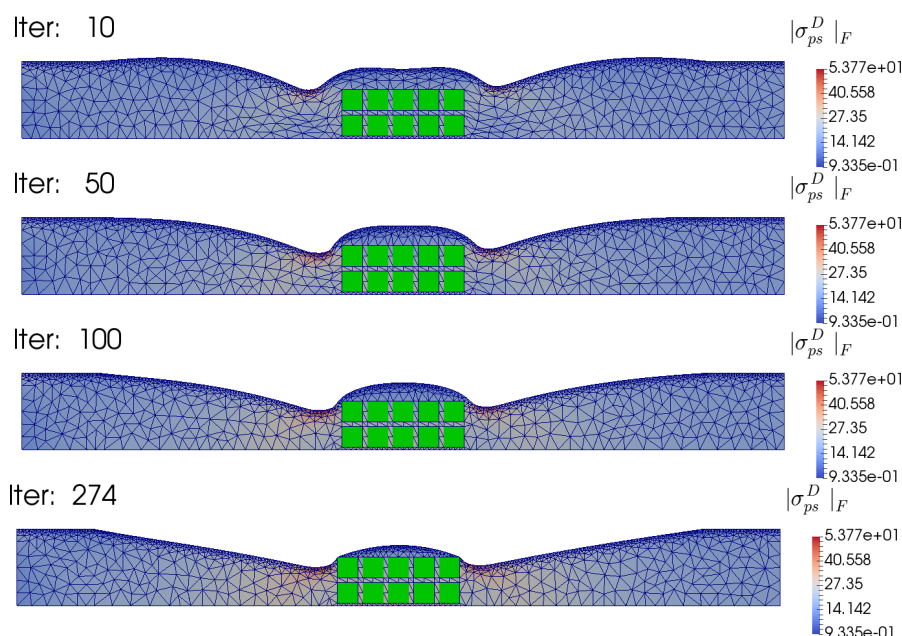FIG. 6. *Experiment* 1: *specimen shapes at gradient descent iterations* 10, 50, 100, *and* 274 *when both* (λ, μ) *are parameters of interest. The color code shows the value of the von Mises stress* $|\boldsymbol{\sigma}_{ps}^{D}|_F$.

allowable stress was set to $\sigma_{\max} = 52\,\text{N/mm}^2$ in each case. For comparison, the yield stress of polycarbonate is described in the literature to lie between $55\,\text{N/mm}^2$ and $75\,\text{N/mm}^2$.

4.1. Experiment 1: Joint parameter identification. In this first experiment we consider the OED shape optimization problem for the case when both Lamé parameters (λ, μ) in (2.5) are to be identified from a single experiment. The initial shape is as in Figure 3 and some snapshots showing the domain in gradient descent iterations 10, 50, 100 and in the final iteration 274 are shown in Figure 6.

Figure 5 shows the evolution of the objective function, the Armijo step sizes and the relative change of the marginal confidence intervals (2.18b) over the iterations.

Remeshing (depicted by gray vertical lines) is triggered in iterations 15, 91, 151, 181, and 241. The horizontal lines illustrate the minimum and maximum values of the quantity shown in the respective graph.

4.2. Experiment 2: Single parameter identification. In the second set of experiments we consider the identification of *either* λ *or* μ with the other parameter assumed known. These experiments are provided for two reasons. First, optimized shapes are easier to interpret from an application point of view when only one parameter is to be identified from the tensile experiment. Second, these experiments show that optimized shapes may depend strongly on the parameter set to be identified.

The situation under consideration is described in subsection 3.3 as case 1. The initial shape is the same as in subsection 4.1; see Figure 3. The final shape in case of the first Lamé parameter λ is shown in Figure 7, which was achieved after 134 iterations. For the final shape of the second Lamé parameter μ obtained after 134 iterations; see Figure 8. Once again we refer the reader to Table 2 for the penalty and stopping parameters in place.
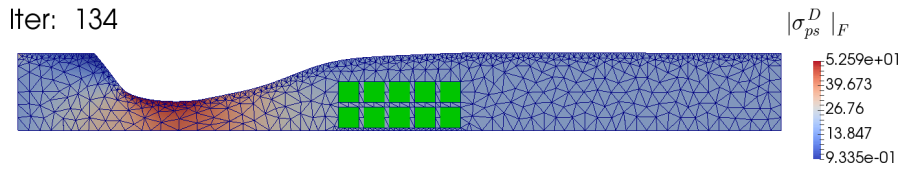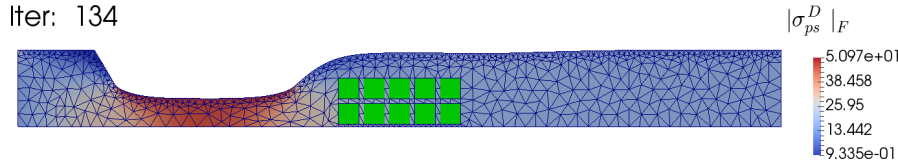
FIG. 7. *Experiment 2: the final shape at gradient descent iteration 134 with λ as the single parameter of interest. The color code shows the value of the von Mises stress $|\boldsymbol{\sigma}_{ps}^D|_F$.*

FIG. 8. *Experiment 2: the final shape at gradient descent iteration 134 with μ as the single parameter of interest. The color code shows the value of the von Mises stress $|\boldsymbol{\sigma}_{ps}^D|_F$.*

4.3. Discussion. Comparing the two final shapes, Figures 7 and 8 for the single parameter identification problems from subsection 4.2, we observe similar optimized shapes, both of which exhibit a thinning of the specimen between the left (clamping) boundary and the measurement regions. This was to be expected since for tensile experiments with constant force, a thinner geometry to the left of the measurement regions will lead to them being displaced more particularly in the horizontal direction, which in turn results in a smaller influence of the measurement errors in the parameter estimation. Notice that the amount of thinning is limited due to the stress penalty condition.

The shape of the optimized specimen changes significantly when both Lamé parameters (λ, μ) are to be identified from a single experiment; see subsection 4.1. In this case, the specimen undergoes thinning both to the left and the right of the measurement regions; see Figure 6. This shape leads to larger relative vertical displacements between individual measurement regions. Besides measurements in horizontal directions, independent vertical displacements gain importance in the two-parameter identification case.

Next we investigate the merit of using optimized specimens. To this end, we compare the radii of the marginal confidence intervals (2.18b) for each parameter between the initial and final shapes. As can be seen from the first row in Table 3, both intervals reduce to about 65% of their original sizes. We also mention Figure 5 (bottom row), where we show the evolution of the relative interval lengths over iteration number. Notice that for any two given shapes of the specimen, the relative dimensions of the confidence intervals do not depend on the confidence level α nor on the value of the constant measurement variance $\sigma_k \equiv \sigma$. Speaking in absolute terms, the marginal confidence radii for λ and μ (for $\sigma_k \equiv 0.1\,\text{mm}$ and $\alpha = 90\%$) decrease from approximately $2200\,\text{N/mm}^2$ to approximately $1400\,\text{N/mm}^2$, respectively, from $400\,\text{N/mm}^2$ to $260\,\text{N/mm}^2$. Keep in mind that the magnitude of both parameters in (4.1) is almost the same. This shows that the experiment (whether optimized or not) yields a higher precision for the second Lamé parameter μ.

This observation remains true for the single-parameter identification experiments. As can be seen from the second and third rows and Table 3, the radius of the confidence interval for μ with optimized specimen is of order $25\,\text{N/mm}^2$ and thus much smaller than the respective radius for λ, which is $150\,\text{N/mm}^2$.

TABLE 3

Summary of results for the 3 parameter identification cases (λ, μ), λ, and μ considered in subsections subsections 4.1 and 4.2. Initial and final values of the first (OED-related) part of the objective are shown along with the radius of the (marginal) confidence interval according to (2.18b) (first row) and (2.18a) (second and third rows) for each parameter in mm, for confidence level $\alpha = 90\%$.

Parameters	ϵ	Final iteration	Initial Ψ_{OED}	Final Ψ_{OED}	Initial CI_λ	Final CI_λ	Initial CI_μ	Final CI_μ
(λ, μ)	1e−5	274	8.9e5	3.8e5	2.2e3	1.4e3	4.0e2	2.6e2
λ	1e−5	134	2.4e4	8.7e3	2.6e2	1.5e2	–	–
μ	1e−5	134	8.5e2	2.3e2	–	–	4.8e1	2.5e1

5. Conclusions and outlook. In this paper we consider the shape of a specimen as an experimental condition in OED problems for linear PDE models. We are aware of only one contribution [19] where this idea has appeared previously in the literature. Our emphasis was to advance this problem class, to derive the Eulerian derivative for a typical OED objective and a meaningful experiment, and to demonstrate that shape optimization has the potential to improve the accuracy of parameter identification tasks. From the practical point of view our model problem is rather elementary and the identification of Lamé parameters is well understood by practitioners. Nevertheless the shape optimization of specimens leads to interesting results, even though the effort of obtaining the formula for the Eulerian derivative is not negligible.

Many extensions of the considered problem come to mind, motivated by practical considerations or mathematical aspects. One may consider, for instance, different types of measurements such as strain gauges, or based on image correlation. The positions of the measurement regions or strain gauges may be optimized as well, along with the tension forces. In place of our stress-driven experiment, one might consider a strain-driven model where the displacement of the boundary is prescribed. So far we assumed the variance of each measurement to be constant. As discussed in subsection 4.3, this gave rise to thinned geometries (see Figures 7 and 8). In practice, the measurement variance may be constant relative to the size of the quantity measured. Taking this into consideration would lead to additional nonlinear dependencies in the objective and in the Eulerian derivative.

As is usual in nonlinear parameter estimation problems, the optimal experiment depends on the value of the unknown parameter. In our setting, optimized shapes depend on the value of (λ, μ). This paradox can be resolved by considering multiple, sequentially designed experiments which take into account intermediate updates of the unknown parameter. Alternatively one may formulate an OED problem which is robust in the value of the parameter. Both approaches can be applied when the shape is used as an experimental condition, but this is outside the scope of this paper.

The criteria (2.17) commonly used in OED problems refer to the size of the confidence ellipsoid in absolute terms. When the parameters are vastly different in size, this may be inappropriate since the optimization will target mostly the confidence of the parameter subvector of largest magnitude. Hence a scaling of the parameters should be introduced.

An extension to 3D geometries with measurements on the boundary of the specimen may offer further potential for optimization due to an increased complexity of possible shapes. However symmetries dictated by the experimental equipment must be taken into account. And finally we expect that nonlinear material laws such as those arising in large-deformation elasticity, or inelasticity, offer a significantly higher

potential for OED techniques since in this realm meaningful experiments can be intricate and less obvious to practitioners. The techniques developed in this paper can be extended to such nonlinear PDEs models. This will incur, besides analytical challenges, further dependencies in the forward, sensitivity, and adjoint equations. The details are left for future research.

REFERENCES

[1] M. BAMBACH, M. HEINKENSCHLOSS, AND M. HERTY, *A method for model identification and parameter estimation*, Inverse Problems, 29 (2013), 025009, https://doi.org/10.1088/0266-5611/29/2/025009.

[2] H. G. BOCK, S. KÖRKEL, AND J. P. SCHLÖDER, *Parameter Estimation and Optimum Experimental Design for Differential Equation Models*, in Model Based Parameter Estimation, Contributions in Mathematical and Computational Sciences 4, Springer, New York, 2013, pp. 1–30, https://doi.org/10.1007/978-3-642-30367-8_1.

[3] M. BONNET AND A. CONSTANTINESCU, *Inverse problems in elasticity*, Inverse Problems, 21 (2005), pp. R1–R50, https://doi.org/10.1088/0266-5611/21/2/R01.

[4] T. CARRARO, *Parameter Estimation and Optimal Experimental Design in Flow Reactors*, Ph.D. thesis, University of Heidelberg, 2005, http://nbn-resolving.de/urn/resolver.pl?urn=urn:nbn:de:bsz:16-opus-61141.

[5] J. CÉA, *Conception optimale ou identification de formes: Calcul rapide de la dérivée directionnelle de la fonction coût*, RAIRO Modél. Math. Anal. Numér., 20 (1986), pp. 371–402, https://doi.org/10.1051/m2an/1986200303711.

[6] J. DAVIS, *Tensile Testing*, 2nd ed., ASM International, Materials Park, OH, 2004.

[7] M. C. DELFOUR AND J.-P. ZOLÉSIO, *Shape sensitivity analysis via min max differentiability*, SIAM J. Control Optim., 26 (1988), pp. 834–862, https://doi.org/10.1137/0326048.

[8] K. EPPLER, *On Hadamard Shape Gradient Representations in Linear Elasticity*, Technical report SPP1253-104, Priority Program 1253, German Research Foundation, 2010, http://www.am.uni-erlangen.de/home/spp1253/wiki/index.php/Preprints.

[9] V. V. FEDOROV AND S. L. LEONOV, *Optimal Design for Nonlinear Response Models*, Chapman & Hall/CRC Biostat. Ser., CRC Press, Boca Raton, FL, 2014.

[10] E. HABER, L. HORESH, AND L. TENORIO, *Numerical methods for experimental design of large-scale linear ill-posed inverse problems*, Inverse Problems, 24 (2008), 055012, https://doi.org/10.1088/0266-5611/24/5/055012.

[11] R. HERZOG AND F. OSPALD, *Parameter identification for short fiber-reinforced plastics using optimal experimental design*, Internat. J. Numer. Methods Engrg., 110 (2017), pp. 703–725, https://doi.org/10.1002/nme.5371.

[12] R. HERZOG AND I. RIEDEL, *Sequentially optimal sensor placement in thermoelastic models for real time applications*, Optim. Eng., 16 (2015), pp. 737–766, https://doi.org/10.1007/s11081-015-9275-0.

[13] R. HIPTMAIR, A. PAGANINI, AND S. SARGHEINI, *Comparison of approximate shape gradients*, BIT, 55 (2015), pp. 459–485, https://doi.org/10.1007/s10543-014-0515-z.

[14] K. ITO AND K. KUNISCH, *Maximizing robustness in nonlinear ill-posed inverse problems*, SIAM J. Control Optim., 33 (1995), pp. 643–666, https://doi.org/10.1137/S0363012992230982.

[15] S. KÖRKEL, I. BAUER, H. G. BOCK, AND J. SCHLÖDER, *A Sequential Approach for Nonlinear Optimum Experimental Design in DAE Systems*, in Scientific Computing in Chemical Engineering II, Springer, New York, 1999, pp. 338–345.

[16] S. KÖRKEL, E. KOSTINA, H. G. BOCK, AND J. P. SCHLÖDER, *Numerical methods for optimal control problems in design of robust optimal experiments for nonlinear dynamic processes*, Optim. Methods Softw., 19 (2004), pp. 327–338, https://doi.org/10.1080/10556780410001683078.

[17] T. LAHMER, B. KALTENBACHER, AND V. SCHULZ, *Optimal measurement selection for piezo-electric material tensor identification*, Inverse Probl. Sci. Eng., 16 (2008), pp. 369–387, https://doi.org/10.1080/17415970701743368.

[18] A. LAURAIN AND K. STURM, *Distributed shape derivative via averaged adjoint method and applications*, ESAIM Math. Model. Numer. Anal., 50 (2016), pp. 1241–1267, https://doi.org/10.1051/m2an/2015075.

[19] D. Logashenko, B. Maar, V. Schulz, and G. Wittum, *Optimal geometrical design of Bingham parameter measurement devices*, in Fast Solution of Discretized Optimization Problems, Internat. Ser. Numer. Math. 138, Birkhäuser, Basel, 2001, pp. 167–183.

[20] A. Logg, K.-A. Mardal, G. N. Wells, et al., *Automated Solution of Differential Equations by the Finite Element Method*, Springer, New York, 2012, https://doi.org/10.1007/978-3-642-23099-8.

[21] J. Nocedal and S. Wright, *Numerical Optimization*, 2nd ed., Springer, New York, 2006, https://doi.org/10.1007/978-0-387-40065-5.

[22] L. Pronzato and A. Pázman, *Design of Experiments in Nonlinear Models: Asymptotic Normality, Optimality Criteria and Small-Sample Properties*, Lecture Notes in Statist. 212, Springer, New York, 2013, https://doi.org/10.1007/978-1-4614-6363-4.

[23] F. Pukelsheim, *Optimal Design of Experiments*, Classics Appl. Math. 50, SIAM, Philadelphia, 2006.

[24] V. Schulz and M. Siebenborn, *Computational comparison of surface metrics for PDE constrained shape optimization*, Computat. Methods Appl. Math., 16 (2016), pp. 485–496, https://doi.org/10.1515/cmam-2016-0009.

[25] V. H. Schulz, M. Siebenborn, and K. Welker, *Efficient PDE constrained shape optimization based on Steklov–Poincaré type metrics*, SIAM J. Optim., 26 (2016), pp. 2800–2819.

[26] D. Skanda and D. Lebiedz, *An optimal experimental design approach to model discrimination in dynamic biochemical systems*, Bioinformatics, 26 (2010), pp. 939–945, https://doi.org/10.1093/bioinformatics/btq074.

[27] J. Sokołowski and J.-P. Zolésio, *Introduction to Shape Optimization*, Springer, New York, 1992.

[28] M. Sonntag, S. Schmidt, and N. R. Gauger, *Shape derivatives for the compressible Navier–Stokes equations in variational form*, J. Comput. Appl. Math., 296 (2016), pp. 334–351, https://doi.org/10.1016/j.cam.2015.09.010.

[29] K. Sturm, *Minimax Lagrangian approach to the differentiability of nonlinear PDE constrained shape functions without saddle point assumptions*, SIAM J. Control Optim., 53 (2015), pp. 2017–2039, https://doi.org/10.1137/130930807.

[30] D. Uciński, *Optimal Measurement Methods for Distributed Parameter System Identification*, Syst. Control Ser., CRC Press, Boca Raton, FL, 2005.